Crystal and Electronic Structures of Complex Bismuth Iodides $A_3Bi_2I_9$ (A = K, Rb, Cs) Related to Perovskite: Aiding the Rational Design of Photovoltaics

Anna J. Lehner,[*,†,‡] Douglas H. Fabini,[¶,‡] Hayden A. Evans,[§,‡]
Claire-Alice Hébert,[‖] Sara R. Smock,[§] Jerry Hu,[‡] Hengbin Wang,[†]
Josef W. Zwanziger,[⊥,#] Michael L. Chabinyc,[†,¶,‡] and Ram Seshadri[†,‡,¶,§]

Mitsubishi Chemical Center for Advanced Materials, Materials Research Laboratory, Materials Department, Department of Chemistry and Biochemistry, College of Creative Studies, University of California, Santa Barbara CA 93106, United States, Department of Chemistry, Dalhousie University, Halifax, NS B3H 4R2, Canada, and Institute for Research in Materials, Dalhousie University, Halifax, NS B3H 4R2, Canada

E-mail: alehner@mrl.ucsb.edu

---

[*] To whom correspondence should be addressed
[†] Mitsubishi Chemical Center for Advanced Materials
[‡] Materials Research Laboratory
[¶] Materials Department
[§] Department of Chemistry and Biochemistry
[‖] College of Creative Studies, University of California, Santa Barbara CA 93106, United States
[⊥] Department of Chemistry, Dalhousie University, Halifax, NS B3H 4R2, Canada
[#] Institute for Research in Materials, Dalhousie University, Halifax, NS B3H 4R2, Canada

Abstract

Ternary bismuth halides form an interesting functional materials class in the context of the closely related Pb halide perovskite photovoltaics, especially given the significantly reduced toxicity of Bi when compared with Pb. The compounds $A_3Bi_2I_9$ (A = K, Rb, Cs) examined here crystallize in two different structure types: the layered defect-perovskite $K_3Bi_2I_9$ type, and the $Cs_3Cr_2Cl_9$ type. The latter structure type features isolated $Bi_2I_9^{3-}$ anions. Here the crystal structures of the ternary iodides are redetermined and a corrected structural model for $Rb_3Bi_2I_9$, as established by single crystal X-ray diffraction and solid state ^{87}Rb nuclear magnetic resonance (NMR) spectroscopy and supported by Density Functional Theory (DFT) calculations is presented. A variety of facile preparation techniques for single crystals, bulk materials, as well as solution-processed thin films are described. The optical properties and electronic structures are investigated experimentally, by optical absorption and ultraviolet photoemission spectroscopy, and computationally by DFT calculations. Absolute band positions of the valence and conduction bands of these semiconductors — with excellent agreement of experimental and calculated values — are reported, constituting a useful input for the rational interface design of efficient electronic and optoelectronic devices. The different structural connectivity in the two different structure types, somewhat surprisingly, appears to not impact band positions or band gaps in a significant manner. Computed dielectric properties, including the finding of anomalously large Born effective charge tensors on Bi^{3+}, suggest proximal structural instabilities arising from the Bi^{3+} $6s^2$ lone pair. These anomalous Born effective charges are promising for defect screening and effective charge carrier transport. The structural, electronic, and optical properties of the complex bismuth iodides are to some extent similar to the related lead iodide perovskites. The deeper valence band positions in the complex bismuth iodides points to the need for different choices of hole transport materials for Bi-iodide based solar cell architectures.

1 Introduction

Heavy metal halide semiconductors have been intensely investigated over the last decades, due to their rich structural chemistry and interesting optical and electronic properties. Recently, photovoltaic applications of tetrel halides such as Ge,[1] Sn,[2,3] and most prominently Pb halide perovskites[4,5] have attracted tremendous interest. In comparison, the optoelectronic properties of bismuth halides have been the focus of many fewer studies. The simple iodide BiI_3 has been investigated for applications such as hard radiation detection,[6–9] X-ray imaging,[10–12] and for solar cells as hole transport material.[13] Recently, some of us have demostrated that BiI_3 can be used as the active layer in photovoltaic devices.[14] Hybrid organic-inorganic bismuth halides have been studied regarding their rich structural variety[15,16] and in some cases optical properties.[17–19] Despite their much simpler composition, the optoelectronic properties of the ternary inorganic bismuth halides, with their most common family being the enneahalogenidometallate phases $A_3Bi_2X_9$ (A = K, Rb, Cs, or Tl; X = halide), have not been explored as extensively. Here we focus on the heavy alkali metal bismuth iodides $A_3Bi_2I_9$ for which the crystal structures have been reported: A = K,[20] Rb,[21] and Cs.[22] While the phase transitions in the Cs compound have been well-studied,[23–26] only one report each for the K and Rb salt are to be found.

It is typical for the extensive family of $A_3M_2X_9$ structures that A and X atoms are closest packing and the M atoms occupy $2/3$ of the octahedral X_6 voids.[24,27,28] Two main structure types of $A_3M_2X_9$ can be distinguished, the ones with hexagonal close packing and the ones with cubic close packing of A and X. For the bismuth iodides of the former group, isolated $Bi_2I_9^{3-}$ ions result as pairs of face-sharing Bi-I octahedra (*e.g.* $Cs_3Cr_2Cl_9$ type $Cs_3Bi_2I_9$) and for the latter, defect-perovskites, corrugated layers of Bi-I octahedra are present (*e.g.* $K_3Bi_2I_9$). As the 6s lone-pair-bearing Bi^{3+} is isoelectronic to the tetrel dications and soft or polarizable just as Pb^{2+}, the bismuth halide crystal chemistry is similar to the lead halide perovskites: rich structual diversity is observed, including distortion, vacancies, and various modes of aggregation of the MX_6 octahedra.[15] However, Bi^{3+} exhibits a stronger tendency to form structures of lower dimensionality of the metal halide units than Pb^{2+}. Recently, the closely related caesium antimony iodide $Cs_3Sb_2I_9$ has been investigated as solar cell absorber layer and the electronic structure of its polymorphs has been calculated by density functional theory (DFT).[29] In contrast, the investigation of the properties of inorganic bismuth halides has been limited to some work reporting optoelectronic properties[21,30–33] and so far as we can discern, apart from a few calculated parameters for $Cs_3Bi_2I_9$,[34] there are no computational studies of the electronic band structures available. Clearly complex bismuth halides are an interesting family of potentially solution-processable compounds, whose potential as an alternative to toxic lead halides is far from fully explored.

Here we present a combined, systematic experimental and computational study of some complex bismuth iodides, in an attempt to correlate crystal structure, electronic structure, and spectroscopic properties within this interesting materials class. Absolute band positions are derived using spectroscopic and DFT methods as a foundation for the rational design of device interfaces. From the DFT band structure calculations, we discuss band dispersion and bonding character, as well as dielectric response properties as indicators of charge carrier transport. We find the structural, electronic, and optical properties of the complex bismuth iodides to be somewhat similar to the related lead iodide perovskites. The deeper valence band positions in the complex bismuth iodides calls for different choices to be made for hole transport materials in Bi-iodide based solar cell architectures. In the two different structural types reported here, the distinct structural connectivity appears to not impact band positions or band gaps in a significant manner. However, band dispersions are significantly different for the two.

2 Methods

2.1 Materials Preparation

All chemicals were purchased and used as supplied: BiI_3 (Strem 99.999%), HI 57% aqueous solution (Sigma-Aldrich 99.95%), KI (Sigma-Aldrich 99.998%), RbI (Strem 99.8%), and CsI (Strem 99.999%). The following solvents were used in their anhydrous forms: ethanol (Sigma-Aldrich 99.995%), acetonitrile (Sigma-Aldrich 99.8%), diethyl ether (Sigma-Aldrich, 99.0%), and N,N-dimethylformamide (Sigma-Aldrich 99.8%). Red $K_3Bi_2I_9$ crystals of relatively poor quality for single crystal X-ray diffraction were obtained by heating a stoichiometric mixture of the binary iodides in an evacuated sealed fused silica ampoule, following a previously reported protocol.[21] High quality crystals of $Rb_3Bi_2I_9$ and $Cs_3Bi_2I_9$ were obtained through solvothermal reactions. In a typical preparation, the stoichiometric mixture (300 mg) of the iodides BiI_3 and RbI, or CsI, respectively, were suspended in Ethanol (6 cm^3) and heated to 120°C in a pressure vessel (Parr autoclave with 23 cm^3 Teflon liner) for 6 h followed by a slow (5°C/h) cooling to room temperature. Red prisms (A = Rb) or red hexagonal platelets (A = Cs) were isolated by filtration. All materials can be kept in dry air for many days (A = K) to months (A = Cs), before significant crystal degradation and decomposition into the crystalline starting iodides occurs.

Bulk powders of the ternary iodides were prepared by stirring the binary iodides in the stoichiometric ratio in CH_3CN (2 cm^3 for 200 mg of product) for 5 h at room temperature. For the K and Rb salts, the resulting red solution was concentrated under vacuum until little solvent was left over the forming precipitation which was then filtered off. The Cs analogue was filtrated directly from the stock solution. The salts were washed with diethyl ether and their phase purity was confirmed by powder X-ray diffraction. As an alternative new route to the pure $A_3Bi_2I_9$ salts, high-energy ball-milling of AI and Bi_3 in a 3:2 ratio (10 min for 200 mg) using tungsten carbide vials and balls in a Spex SamplePrep 8000D

Dual mixer/mill was successfully applied.

2.2 Characterization Methods

X-ray diffraction data on powder samples (PXRD) was recorded for the K and Cs salts over the 2θ scattering angle range of 6° to 70° using Cu-Kα radiation (Philips X'Pert MPD diffractometer). For the Rb salt (sample diluted with 40w% cubic BN, Alpha Aesar), PXRD data using high-resolution synchrotron radiation was recorded on beamline 11-BM at the Advanced Photon Source, Argonne National Laboratory at 295 K with an average wavelength of $\lambda = 0.458996$ Å. For $K_3Bi_2I_9$ and $Cs_3Bi_2I_9$ samples, the agreement with published crystal structure models (A = K,[21] Cs[22]) was confirmed by Rietveld refinements using TOPAS-Academic V5.[35] X-ray diffraction on single crystals was performed using a Bruker Kappa APEX II diffractometer with a sealed tube Mo-Kα X-ray source. Single crystal samples were mounted onto Nylon loops and fixed with two component epoxy glue. For $Rb_3Bi_2I_9$ a full data set was collected at room temperature by sampling a fraction of the Ewald sphere with 0.5° ω steps, while only lattice parameters were determined for the K and Cs salts. The cell refinement, data reduction, correction, and integration were peformed using Bruker's SAINT/SADABS software[36,37] The structure was solved with Direct methods using SHELXS-97 and the refinement was done using SHELXL-2014.[38,39] We used the program VESTA[40] for the graphical representation of the crystal structures and the thermal ellipsoids where plotted using ORTEP-III.[41] For additional crystal structure data see Supporting Information; further details of the crystal structure investigation may be obtained from FIZ Karlsruhe, 76344 Eggenstein-Leopoldshafen, Germany (fax: (+49)7247-808-666; e-mail: crysdata(at)fiz-karlsruhe(dot)de), on quoting the deposition number CSD-430179. Experimental densities were determined for cold-pressed pellets on a MicroMeritics AccuPyc 1340 pycnometer by performing sensitive volume (by He gas displacement) and mass measurements.

A ^{87}Rb solid state magic angle spinning nuclear magnetic resonance (MAS NMR) single pulse experiment was performed for polycrystalline $Rb_3Bi_2I_9$ on a Bruker AVANCE III 800 MHz (18.8 T) standard bore spectrometer operating at 261.81 MHz with a 2.5 mm zirconia rotor system at a spinning frequency of 30.0 kHz. In order to enhance the signature of the quadrupolar interactions in the spectra, ^{87}Rb triple-quantum magic angle spinning (3QMAS NMR) experiments were performed on a Bruker Avance III HD 400 MHz (9.4 T) WB solid-state NMR spectrometer operating at 130.92 MHz with a 4.0 mm double resonance MAS probe head spinning at 12.5 kHz. Chemical shifts were referenced to a 1 molar aqueous $Rb(NO_3)$ solution using solid RbCl at 127 ppm[42] as a secondary reference. The single pulse experiment was performed with a $\pi/12$ excitation pulse of 0.62 μs using a 3 s relaxation delay, which was optimized for quantitative analysis, a 2.05 ms acquisition time, and an accumulation of 448 scans. The 3QMAS experiment was carried out using a three-pulse MQMAS sequence with a z-filter and the following parameters: an excitation pulse of 4.2 μs, a conversion pulse of 1.4 μs and a weak central transition selective 90° pulse of 20 μs. A States-TPPI phase sensitive detection in the F1 dimension was employed. The quadrupolar central transitions of the ^{87}Rb NMR spectra were simulated and analyzed with the Line Shapes module within the Topspin 3.2 software of Bruker BioSpin.

Scanning electron microscopy (SEM) images of thin film samples sputtered with gold/palladium to limit charging were collected using a FEI XL40 Sirion FEG digital scanning microscope in backscattered electron imaging mode. Optical spectra in the UV-Vis range from 220 to 800 nm were recorded using a Shimadzu UV3600 spectrometer in diffuse reflection on powder samples which were spread thinly onto compacted $BaSO_4$ powder. Diffuse reflection data were converted using the Kubelka-Munk transformation implemented in the spectrometer's software. Band gaps were extracted from Tauc plots[43,44] of the Kubelka-Munk transformed reflection data assuming allowed direct or indirect lowest energy transitions depending on the results from our DFT calculations. A Kratos Axis Ultra XPS/UPS instrument was used for X-ray and Ultraviolet Photoelectron Spectroscopy (XPS and UPS). Samples were prepared by dropcasting and spincoating from dimethylformamide or acetonitrile solution as thin films on 10×10 mm pieces of silicon wafers onto which 20 nm of chromium and 90 nm of gold had been deposited by thermal evaporation under high vacuum (10^{-7} torr). Material was removed from one edge of each sample via swabbing with chlorobenzene to expose the gold layer. Nickel tape was used to electrically connect the exposed gold on the top of the substrates to the airtight sample holder which was loaded in a glove box (N_2, $\leq$1 ppm O_2). For XPS, a monochromated Al-Kα source (180 W) was used under ultrahigh-vacuum conditions (10^{-8} torr). Survey scans were collected with a step size of 500 meV, a pass energy of 160 eV, and a dwell time of 150 ms. For UPS, a helium I radiation source was used with a gate bias voltage of -9 V. Photoelectrons at the 0° takeoff angle were collected at 600 W (6 kV, 10 mA) with a pass energy of 5 eV and a step size of 25 meV. Survey scans were collected once with a dwell time of 150 ms. Detailed scans near the valence band maximum (VBM) were collected with a dwell time of 600 ms and were repeated 3 times. The position of the VBM was determined from UPS spectra as the energy increment between the left and right edges of the spectral feature, subtracted from the incident photon energy (21.22 eV).

2.3 Computational Methods

The DFT computational study of the electronic band structures, including absolute band positions, was carried out using the Vienna *ab initio* Simulation Package (VASP).[45–48] VASP implements density functional theory in the Kohn-Sham formulation, using a plane wave basis and the projector-augmented wave formalism (PAW).[49,50] Input structures were taken from the literature for $K_3Bi_2I_9$[21] and $Cs_3Bi_2I_9$,[22] and from this work for $Rb_3Bi_2I_9$. For a better comparability of the band structures, the monoclinic phases were transformed to the space group setting $P2_1/c$ and the corresponding high-symmetry points were selected for the corresponding conventional Brillouin zone.[51] All ternary compounds were optimized using the Perdew-Burke-Ernzerhof (PBE) exchange and correlation functional[52] until the residual forces were less than 0.01 eV/Å on each atomic site. The resulting crystal structures exhibited 8 to 10% increased volumes compared to the experimental input structures, which lies withing the acceptable range of errors of the applied method. The energy cut-off of the plane wave basis set was 500 eV. A Gamma centered k-mesh grid with a minimum of 20 k-points was employed with the convergence criteria set at 0.01 meV. The band structures were calculated using PBE including spin-orbit coupling (SOC) in order to locate the band gap, but for more accurate band gap values and density of states (DOS), a screened hybrid functional (HSE06)[53,54] with SOC was employed.

Absolute band positions for the ternary compounds were obtained by aligning the s-like states of Bi in $A_3Bi_2I_9$ from HSE+SOC DOS calculations to the corresponding levels of BiI_3 as derived by a slab calculation[55] of a 1×1×4 half-filled supercell (PBE+SOC, see our previous work[56] for computational details). Born effective charge tensors (Z^*_{ij}) on Bi^{3+} and high-frequency (ion-clamped) dielectric constants (ϵ^{∞}_{ij}) were calculated as reported previously.[56] Calculations of those dielectric response parameters for the related binary iodides PbI_2[56] using different computational schemes revealed that PBE+SOC is sufficient to reproduce values very close to the more accurate but computationally much more demanding HSE06+SOC. In the present work however, PBE without SOC was applied for the monoclinic systems to reduce computation time. Computations of the NMR observables for two structure models of $Rb_3Bi_2I_9$, this work's model in $P2_1/n$ and the Pc model reported by Sidey *et al.*,[20] were performed with the plane wave and PAW-based QUANTUM ESPRESSO package[57] together with the QE-GIPAW extension. QE-GIPAW computes the magnetic shielding at each nucleus using the gauge-including projector augmented wave formalism,[58,59] and the electric field gradient at each nuclear site using standard PAW expressions.[60] PAW atomic datasets for Rb, Bi, and I were used based on the set recently published by Jollet, Holzwarth, and Torrent, and generated with the ATOMPAW code to create files suitable for QUANTUM ESPRESSO.[61,62] Cut-off radii of 2.30, 2.90, and 2.30 Bohr were used for Rb, Bi, and I respectively; these are short enough that no PAW sphere overlap occurred. The PBE exchange and correlation functionals were used in all cases and the structures were computed with the experimental atomic positions and no subsequent optimization. Complete convergence required a planewave cut-off energy of 80 Ry (1088 eV) and a reciprocal point grid spacing of 0.02 Å^{-1}; however, as these values led to prohibitively large calculations for chemical shielding on the $Rb_3Bi_2I_9$ system, the values reported here were computed with a cut-off energy of 20 Ry (272 eV) and reciprocal point spacing of 0.04 Å^{-1}. To check that these more modest values were sufficient, we computed the chemical shieldings for the rubidium alkali salts at both the fully converged levels and at the more modest levels used here, and found that the shift orderings were still correctly represented and that the systematic error of the PBE functional for chemical shielding calculations was essentially unchanged. This result means that our computation of observables for $Rb_3Bi_2I_9$, even at modest convergence criteria, is useful for establishing experimental peak assignments and for differentiating between different potential crystal structure models.

3 Results and Discussion

3.1 Materials Preparation and Structure

In this work we have established a variety of new facile preparation routes for the ternary bismuth iodides $A_3Bi_2I_9$ (A = K, Rb, Cs). By reacting the corresponding binary iodides in stoichiometric ratio in organic solvents at room temperature or simply ball-milling them, high purity materials were obtained. Previously, methods for growing single crystals, typically at high temperatures from the melts, have been reported.[20,21,23] We have found that single crystals of up to 1 mm can also be obtained at very mild solvothermal conditions in ethanol at 120°C for A = Rb, Cs. As the solubility of the ternary bismuth iodides decreases rapidly with increasing counter cation size, the Cs salt could be isolated directly by filtration of a acetronitrile solution of the starting iodides. For the isolation of powders of the K and Rb salts, the solution was concentrated under vacuum prior to filtration. Thin films were deposited from organic solvents by drop-casting or spin-coating. In future work, the procedures must be carefully optimized to improve microstructure, grain orientation and film quality, but generally the solution-processibility makes this family of heavy metal halides very appealing for technological applications. In this work, the crystal structures were determined for powder and single crystal samples and optoelectronic properties were examined for powders (UV-Vis) and thin films (XPS, UPS), respectively.

The stability in ambient atmosphere has been monitored by PXRD on as-prepared polycrystalline powder samples. With increasing size of the counter cation, the salts kept well for hours (K) to months (Cs) in ambient air, which is considerably longer than the extremely oxidation sensitive Sn^{2+} iodides or the moisture sensitive Pb^{2+} iodides would withstand. Exploring the effects of other factors on the stability, such as different grain sizes and thus surface areas as a result of different preparation processes, will be an important future task. Our preliminary studies have confirmed that phase widths of mixed counter cations K-Rb, Rb-Cs, K-Cs exist in the $A_3Bi_2I_9$ phases. Taking into account not only the counter cation but also the variability of the central metal and halide, which has been previously explored only in some extent,[63] this rich family of compounds offers a large variety of new interesting phases with tunable properties.

The crystal structures of the three ternary bismuth iodides $A_3Bi_2I_9$ (A = K, Rb, Cs) were examined by X-ray diffraction. Unit cell dimensions were derived from single crystal measurements and the phase purity was confirmed by Rietveld refinements of powder diffraction data (see Figure 1, Table 1, 2, and Supporting Information). For all three phases, the densities calculated from the structural data correspond nicely to the experimental densities which were determined by He gas displacement measurements (Supporting Information). For $K_3Bi_2I_9$[21] and $Cs_3Bi_2I_9$,[22] an excellent agreement with previous crystal structure reports was obtained, while the redetermination of the structure of $Rb_3Bi_2I_9$ led to a new structure model with the space group $P2_1/n$ instead of the previously reported model in space group Pc.[20] From X-ray diffraction of $Rb_3Bi_2I_9$ single crystals, this space group

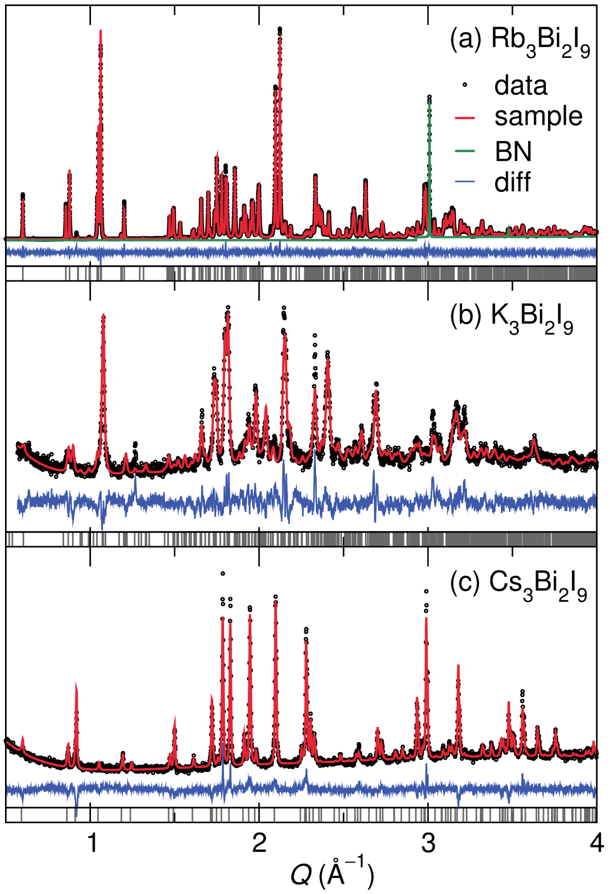

Figure 1: Powder X-ray diffraction and Rietveld refinements of $A_3Bi_2I_9$, A = (a) Rb (synchrotron data), (b) K, and (c) Cs (laboratory data).

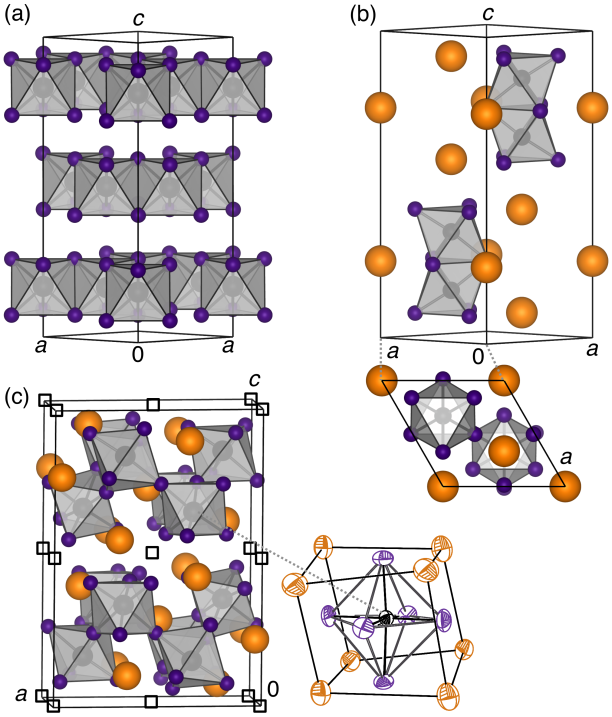

Figure 2: Crystal structures of (a) BiI_3 ($R\bar{3}$),[64] (b) $Cs_3Bi_2I_9$ ($P6_3/mmc$),[22] and (c) $Rb_3Bi_2I_9$ ($P2_1/n$) with empty squares marking the unoccupied metal positions of the perovskite aristotype. Small spheres represent I^-, large spheres are counter cations A^+, and spheres inside polyhedra are Bi^{3+}. The close relationship to the perovskite structure is obvious from the coordination environment of the BiI_6 octahedra (Ortep plot with ellipsoids at 80%).

Table 1: Crystallographic parameters of $Rb_3Bi_2I_9$ with experimental densities derived from gas displacement pycnometry included for comparison.

Formula	$Rb_3Bi_2I_9$
Sample	single crystal
Structure type	$K_3Bi_2I_9$ [21]
Crystal system	monoclinic
Space group	$P2_1/n$
Unit cell (Å,°)	
A	14.6443(19)
b	8.1787(9)
c	20.885(2)
β	90.421(7)
V (Å^3)	2501.4(5)
Z	4
Density (X-ray) (g/cm^3)	4.82
Density (Pycnom.) (g/cm^3)	4.82(2)
X-ray λ (Å)	0.71073
Diffractometer	Bruker Apex II
T (K)	299(2)
Absorption coefficient	30.9
2Θ range (°)	3.4 to 56.8
No. measured reflections	18931
No. unique reflections	6269
R_{int}	0.0464
No. free parameters	127
Goodness of fit F^2	1.018
*R*1, *wR*2 ($I \geq 2\sigma(I)$)	0.0409 0.0879
*R*1, *wR*2 (all reflections)	0.0791, 0.1001
Residual e$^-$ density (e$^-$Å^3)	1.62 /$-$1.93

Table 2: Wyckoff positions, coordinates, and equivalent isotropic displacement parameters U_{eq} (Å^2) in the crystal structure of $Rb_3Bi_2I_9$ ($P2_1/n$).

Atom	Wyckoff site	x	y	z	U_{eq}
Rb(1)	4*e*	0.03098(9)	0.97581(2)	0.22393(8)	0.0622(4)
Rb(2)	4*e*	0.18643(1)	0.52117(2)	0.06266(8)	0.0721(4)
Rb(3)	4*e*	0.35098(1)	0.97172(1)	0.89373(8)	0.0692(4)
Bi(1)	4*e*	0.16689(2)	0.49351(4)	0.84409(2)	0.0276(1)
Bi(2)	4*e*	0.33675(2)	0.01025(4)	0.15456(2)	0.0278(1)
I(1)	4*e*	0.00492(5)	0.58289(1)	0.74634(5)	0.0602(3)
I(2)	4*e*	0.07209(5)	0.80753(9)	0.38965(4)	0.0458(2)
I(3)	4*e*	0.12109(5)	0.79317(9)	0.91443(4)	0.0457(2)
I(4)	4*e*	0.16975(5)	0.06654(1)	0.07954(5)	0.0541(2)
I(5)	4*e*	0.24235(5)	0.69155(9)	0.21872(4)	0.0433(2)
I(6)	4*e*	0.32991(5)	0.42761(1)	0.92177(4)	0.0524(2)
I(7)	4*e*	0.41596(6)	0.80249(9)	0.05562(4)	0.0465(2)
I(8)	4*e*	0.79932(5)	0.82268(9)	0.24451(4)	0.0451(2)
I(9)	4*e*	0.95328(5)	0.70836(9)	0.07647(4)	0.0448(2)

could be clearly derived from the unit cell metrics (a = 14.6443(19), b = 8.1787(9), c = 20.885(2) Å, β = 90.421(7)°), the symmetry (Laue class 2/m) and the systematic zonal and serial extinction conditions ($h0l$ reflections only present for $h+l = 2n$, $h00$ reflections only present for $h = 2n$). The solution of the crystal structure using direct methods led to the expected composition with four formula units per unit cell and all atoms occupying general positions (Wyckoff sites 4*e*). Using anisotropic thermal displacement parameters, the structure model was refined to a good fit and reliable $R1$ value in few iterations. The final values of the positional and displacement parameters are listed in Table 2. Additional structural data as well as information about the transformation between the group subgroup pair $P2_1/c$ ($P2_1/n$) and Pc are included in the Supporting Information. It is likely that Sidey *et al.*[20] reported the $Rb_3Bi_2I_9$ crystal structure in the acentric space group *Pc* as a consequence of the crystal twinning in the crystal studied. The atomic positions and unit cell derived in this work are very similar to this previously published structure. In the following, the crystal structure of $Rb_3Bi_2I_9$ will be discussed in detail, while the structures of the isotypic $K_3Bi_2I_9$,[21] of $Cs_3Bi_2I_9$ crystallizing with the $Cs_3Cr_2Cl_9$ structure type,[65] and the binary $\mathrm{BiI_3}$ will be only touched on for comparison. The crystal structures discussed here are shown in Figure 2. Rhombohedral $\mathrm{BiI_3}$ (Figure 2a) contains distorted $\mathrm{BiI_6}$ octahedra, which are connected in honeycomb layers via three shared edges each. The anionic species in $\mathrm{Cs_3Bi_2I_9}$ are isolated pairs of face-sharing $\mathrm{BiI_6}$ ocahedra (Figure 2b). $\mathrm{Rb_3Bi_2I_9}$ (Figure 2c) contains corrugated layers of corner-connected $\mathrm{BiI_6}$ octahedra, the complex 2D anion $^{2}_{\infty}\{[\mathrm{BiI}^{\mathrm{t}}_{3}\mathrm{I}^{\mathrm{e}}_{3/2}]^{-1.5}\}$ written in Niggli nomenclature. The crystal structure can be described as distorted defect variant of the perovskite type (*AMX*$_3$), in which only two thirds of the octahedral M sites are occupied: $\mathrm{Rb(Bi_{2/3}\square_{1/3})I_3}$. Every third M layer of the perovskite aristotype in [001] is depleted (Wyckoff sites $2a$ and $2b$ in the monoclinic unit cell). The ordered cubic close packing of Rb and I occurs in such a way that all $\mathrm{BiI_6}$ octahedra are coordinated by eight Rb atoms in the arrangement of a distorted cube; the unit cell of the perovskite type. Wosylus *e*t al. have derived the symmetric group-subgroup relationships between the cubic perovskite and $\mathrm{Tl_3Bi_2I_9}$ which is isotypic to our new model of $\mathrm{Rb_3Bi_2I_9}$.[66] The $\mathrm{BiI_6}$ octahedra of the two crystallographic Bi sites are distorted with three shorter (2.93±1 Å) and three longer (3.20 to 3.25 Å) Bi-I distances, as it is observed for the K and Cs salts as well as for other complex bismuth iodides.[15] For all structure types the shorter Bi-I bonds involve terminal I sites while the longer bonds exist between Bi and μ_2 (or μ_3 for $\mathrm{Cs_3Bi_2I_9}$) I atoms connecting multiple Bi sites. As this distortion is observed in all related structures, no matter if they contain lone-pair-bearing central metals or not (e.g. $\mathrm{Cs_3Y_2I_9}$[67]), we tentatively conclude that the structural distortion is not caused by a stereochemically active 6s lone pair on $\mathrm{Bi^{3+}}$. For $\mathrm{Rb_3Bi_2I_9}$, the Bi-Bi distances between corner-sharing $\mathrm{BiI_6}$ octahedra are about 6.2 Å. For comparison, the bond lengths are about 4.0 Å in the $\mathrm{Bi_2I_9}$ anions (face-sharing $\mathrm{BiI_6}$) of $\mathrm{Cs_3Bi_2I_9}$ and are about 4.4 Å in the layers of $\mathrm{BiI_3}$ (edge-sharing $\mathrm{BiI_6}$). The effect of the $\mathrm{BiI_6}$ bonding mode in the different crystal structures on the optoelectronic properties and electronic structures will be discussed in the following sections. The iodide sites in $\mathrm{Rb_3Bi_2I_9}$ are coordinated by a total of three to five metal sites, counting both Bi and Rb, while the bridging I sites (I1, I5, and I8) display the larger coordination numbers (CN). Due to the relatively small size of the Shannon ionic radius of Rb^+ (CN 6, 1.5 Å[68]) compared to I^- (CN 6, 2.2 Å[68]), the close packing between those ions is irregular, leading to the distorted and tilted BiI_6 octahedra. As a result, the coordination of the Rb cations by I anions is reduced from the cuboctahedral coordination (CN 12) of the perovskite aristotype A sites to CN 8 with Rb-I distances of up to 4.1 Å. The resulting tilting of BiI_6 octahedra is obvious in the decrease of the M-I-M bond angles from the ideal 180° angle in cubic perovskite aristotype to 147 to 153° in $Rb_3Bi_2I_9$ and even smaller angles for $K_3Bi_2I_9$, where the size mismatch of large I^- and small A^+ ions is more pronounced.

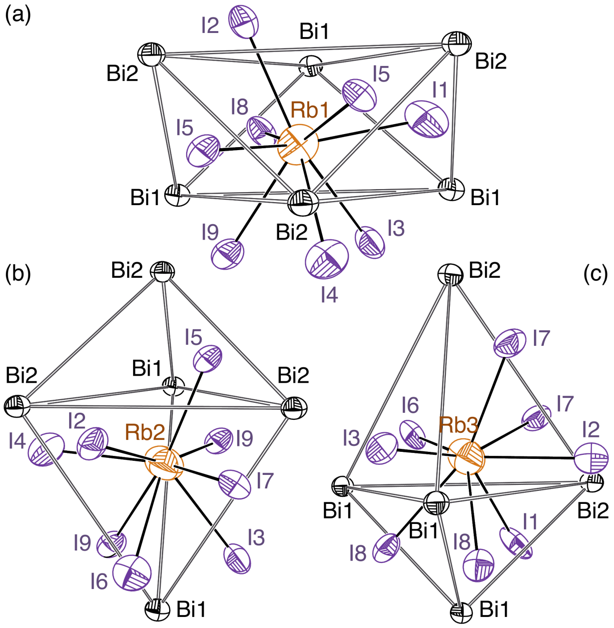

Figure 3: ORTEP plots (ellipsoids at 80% probability level) of the coordination environment of the three Rb sites (a) Rb1, (b) Rb2, (c) Rb3 in $Rb_3Bi_2I_9$ (all on Wyckoff positions 4*e*).

The RbI_8 coordination polyhedra can be described as heavily distorted bicapped trigonal prisms with similar volumes of about 94 Å^3 for all the three Rb sites (Figure 3). In the context of the complete structure, Rb1 sits inside the corrugated layers of BiI_6 octahedra, while Rb2 and Rb3 exhibit local environments similar to each other at the edges of those layers. Thereby, the volume of the trigonal antiprism of Bi sites surrounding Rb1

($CN_{eff}(Rb1Bi_6)$ = 4.6) is about 50% larger than the volume of the trigonal bipyramids of Bi sites coordinating the Rb2 ($CN_{eff}(Rb2Bi_6)$ = 3.3) and Rb3 ($CN_{eff}(Rb3Bi_6)$ = 4.4) sites. Interestingly, the isotope ^{87}Rb is an NMR-active, quadrupolar (spin 3/2) nucleus with approximately 30% natural abundance, which can be probed to reveal the effects of the local structural environment. We examined the NMR signature of the Rb nuclei in $Rb_3Bi_2I_9$ by MAS NMR experiments in combination with DFT-simulation of the NMR observables in order to confirm our centrosymmetric structure model for $Rb_3Bi_2I_9$ as opposed to the previously reported non-centrosymmetric model.

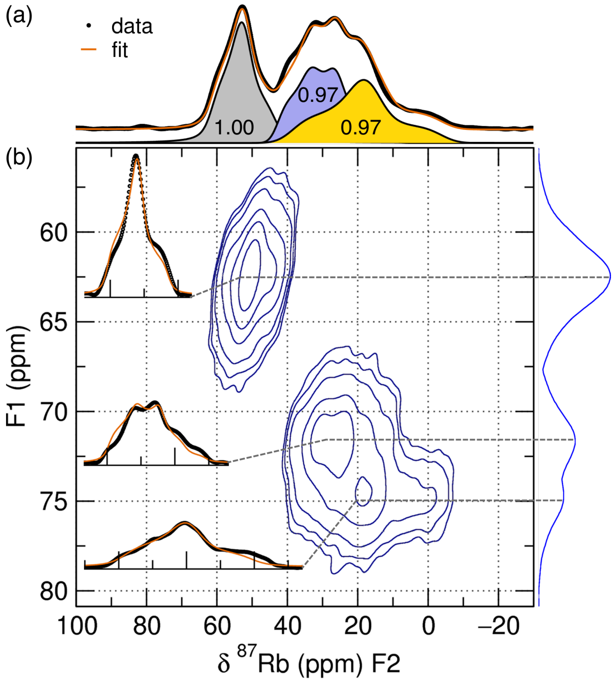

Figure 4: (a)^{87}Rb MQ-MAS NMR spectra of $Rb_3Bi_2I_9$ recorded at 130.92 MHz. The deconvolution of the 1D spectrum (b) into the three Rb sites (see Figure 3) with C_q, η, and δ_{iso} parameters derived from the fits of the individual traces (see Table 3) yields the expected integrated area ratio of 1:1:1 in good agreement.

The NMR spectrum of solid $Rb_3Bi_2I_9$ displays two main features which are broad and overlapping when recorded with a 400 MHz spectrometer (Figure 4). However, the 3QMAS experiment reveals clearly that there are three distinct sites which is in agreement with the three Rb sites of our crystallographic structure model. The traces for each signal obtained from the 3QMAS measurement were fitted with a good agreement to extract

Table 3: Absolute quadrupolar coupling parameters C_q, asymmetry parameters of the quadrupolar interaction η, absolute shielding σ, and isotropic chemical shift δ_{iso} (using RbCl as a reference at 127 ppm[42]) from DFT calculations and NMR experiments for $Rb_3Bi_2I_9$.

Structure	Site	C_q (MHz) calc.	C_q (MHz) exp.	η calc.	η exp.	σ (ppm)	δ_{iso} (ppm) calc.	δ_{iso} (ppm) exp.
$P2_1/n$	Rb1	2.6	2.1	0.91	1.0	1992	41	61
	Rb2	3.9	3.0	0.90	1.0	2016	17	41
	Rb3	3.4	2.8	0.70	0.5	2022	11	44
Pc	Rb1	4.3		0.83		2030	3	
	Rb2	4.3		0.95		1966	67	
	Rb3	3.9		0.43		2051	-18	
	Rb4	3.1		0.55		1962	71	
	Rb5	9.0		0.91		1973	60	
	Rb6	3.9		0.35		1988	45	

NMR parameters which can be simulated by DFT-calculations: the isotropic chemical shift δ_{iso}, the absolute quadrupolar coupling parameter C_q, and the anisotropy parameter of the quadrupolar interaction η (Table 3). Using those parameters, the 1D spectrum could be deconvoluted with a decent fit into three signals (Figure 4a). As expected from the 1:1:1 crystallographic ratio, the integrated areas of those three signals are practically the same (site 1: 1.00, site 2: 0.97, site 3: 0.97). The DFT calculations of the NMR parameters (Table 3) allowed us to compare the NMR signature of our structure model in $P2_1/n$ directly to the non-centrosymmetric Pc structure published by Sidey *et al.*[20] While the calculated chemical shifts for the $P2_1/n$ model are shifted systematically by approximately 25 to 30 ppm compared to the experimental values, the relative shifts differences between the sites are well reproduced. Including the expected shift from the second order quadrupole effect under Magic Spinning does not change this conclusion: using the computed values for C_q in addition to the total shielding again yields a predicted spectrum with two nearly overlapping sites shifted upfield from a third site about 35 ppm downfield. We can thus directly assign the most downfield signal to the Rb1 site (Figure 3a), based on the agreement of experimental and calculated isotropic chemical shift and quadrupolar parameters. As the C_q and η parameters can be calculated with much greater accuracy and reliability than the chemical shift, we use those to assign the signal observed at δ_{iso} = 41 ppm to the Rb2 site and the one at δ_{iso} = 44 ppm to the Rb3 site (Figure 3b,c). For the non-centrosymmetric structure model published in space group Pc, the six sites would give rise to six distinct ^{87}Rb signals spread over a spectral range of over 85 ppm (110 ppm after quadrupole effects are accounted for, see Table 3). This is obviously in stark contrast with our experimental results, which can most clearly be observed in the wide ppm-range section of the single pulse ^{87}Rb MAS NMR spectrum recorded at higher field (Supporting Information). Those results together with our crystallographic studies provide very strong evidence that the correct structure description of $Rb_3Bi_2I_9$ is our centrosymmetric one, which renders this salt strictly isotypic with $K_3Bi_2I_9$[21] and $Tl_3Bi_2I_9$[66] as has been hinted at previously.[66]

3.2 Optical and Electronic Properties

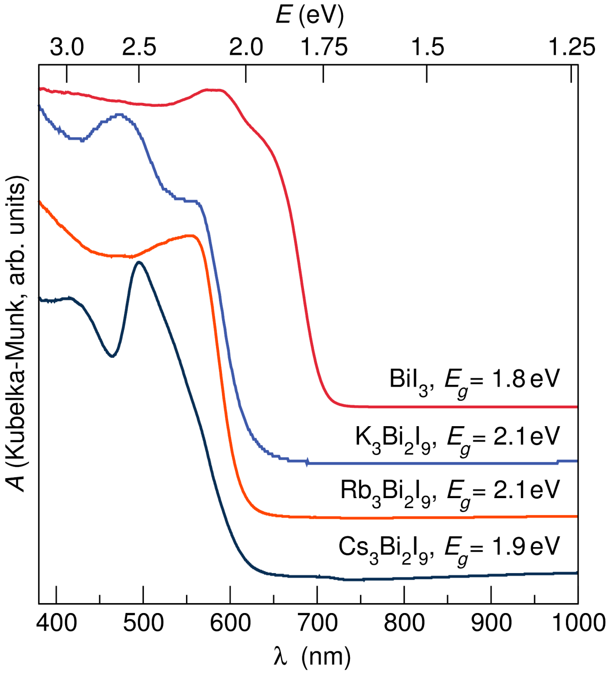

Figure 5: UV-Vis diffuse reflection spectra recorded on powder samples of $A_3Bi_2I_9$ and BiI_3 transformed into absorbance A. Band gaps were obtained using Tauc plots assuming direct gaps for A = K, Rb and indirect gaps for the remaining phases as predicted by DFT calculations (see Table 4).

The optical band gaps of $A_3\mathrm{Bi_2I_9}$ (A = K, Rb, Cs) were derived from Tauc plots of Kubelka-Munk-transformed diffuse reflection UV-Vis data (Figure 5, Table 4). The absorption edge is located at approximately 2 eV for all three ternary bismuth iodides, while the binary exhibits a gap (E_g) of about 1.8 eV. In fact, the variation of the $A_3\mathrm{Bi_2I_9}$ band gaps determined with the given method only stems from the assumption of direct transitions for A = K, Rb, and an indirect transition for A = Cs as taken from the results of our DFT calculations. For the indirect gap $\mathrm{Cs_3Bi_2I_9}$, a smaller band gap results from the Tauc method gap determination, while to the eye, the lighter alkali homologue salts appear a slightly darker red. Those E_g values are in excellent agreement with the values of 1.98 eV for A = Rb and 1.89 eV for A = Cs that were reported previously.[33] In the same study, the descending band gap magnitude of $A_3M_2\mathrm{I_9}$ was correlated with ascending melting points and ascending average atomic numbers. Still, the counter cation, structure type, and thus connectivity mode and dimensionality of the $\mathrm{BiI_6}$ octahedra have very little influence on E_g. The band gap of the layered polymorph of $\mathrm{Cs_3Sb_2I_9}$ of around 2 eV[29] indicates that the variation of the central metal from Bi to Sb also does not have a strong impact on the magnitude of the gap. For the bismuthates, we observe that steepness of the edge, however, is greater for the layered structure types compared to the $\mathrm{Cs_3Bi_2I_9}$ structure containing isolated anions. A steep edge is desirable, as for related lead halide perovskites a steep absorption edge has been correlated to little disorder-induced broadening and the absence of deep optically detectable states.[69]

The ionization energy IE, that is, the position of the valence band maximum (VBM) with respect to the vacuum energy, was determined for the $A_3\mathrm{Bi_2I_9}$ phases by UPS measurements of thin film samples (see $\mathrm{K_3Bi_2I_9}$ example in Figure 6 and Supporting Information for Rb and Cs salts). The sample surface composition was confirmed by XPS prior to recording the UPS spectra. We carried out between three and six UPS measurements of different thin film sample preparations for every compound to gauge the reproducibility and error of this method. The experimentally derived ionization energies are listed in Table 4. VBM deter-

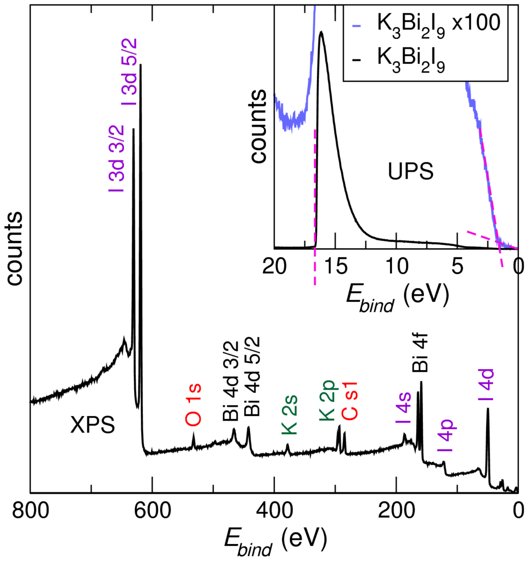

Figure 6: UPS (a) and XPS (b) spectra for $K_3Bi_2I_9$. From XPS data, the surface composition can be determined to $K_{2.84}Bi_2I_{8.95}$ which is in excellent agreement with the expected formula within the scope of the method. From UPS data, the position of the valence band maximum (VBM) was determined by subtracting the energy difference between both edges of the spectral feature from the excitation wavelength (He I lamp, 21.22 eV).

minations by UPS for these relatively wide gap semiconductors are not trivial: Insufficient film coverage leads to signals of the underlying Au layer being captured while measurements on too thick films suffer from charging, both potentially altering the outcomes. For samples with a range of non-detectable to small XPS signals of the underlying gold layer and no to slight charging observed during XPS measurements, the IE values for $A_3Bi_2I_9$ lie between 5.4 eV and 6.4 eV with variations of 0.2 eV to 0.8 eV for each compound.

Table 4: Experimental optical (from diffuse reflection UV-Vis) and calculated (DFT method HSE+SOC) band gaps E_g as well as experimental (from a range of UPS measurements) and calculated ionization energies of $A_3Bi_2I_9$ (A = K, Rb, Cs) and BiI_3.

Phase	E_g (eV)		IE (eV)	
	exp.	calc.	exp.	calc.
BiI_3	1.8	1.93	6.0 to 6.3	6.1
$K_3Bi_2I_9$	2.1	2.17	6.1 to 6.3	6.1
$Rb_3Bi_2I_9$	2.1	2.16	6.1 to 6.2	6.0
$Cs_3Bi_2I_9$	1.9	2.32	5.6 to 6.2	5.7

3.3 Electronic Structure Calculations

In order to support our experimental work with a robust and relatively fast method of determining absolute band positions, we applied DFT calculations to estimate the band positions with respect to the vacuum level. For the binary BiI_3 as a computationally less demanding and closely related proxy, we conducted slab calculations[55] (PBE+SOC, computational details see our previous work[56]) using a half-filled 1×1×4 super-cell to find the absolute VBM position. Details of these calculations have been reported elsewhere.[14] We then aligned deep s-like Bi states of the ternaries' DOS (HSE+SOC) to the corresponding BiI_3 states to obtain absolute VBM positions for all compounds (see Supporting Information).

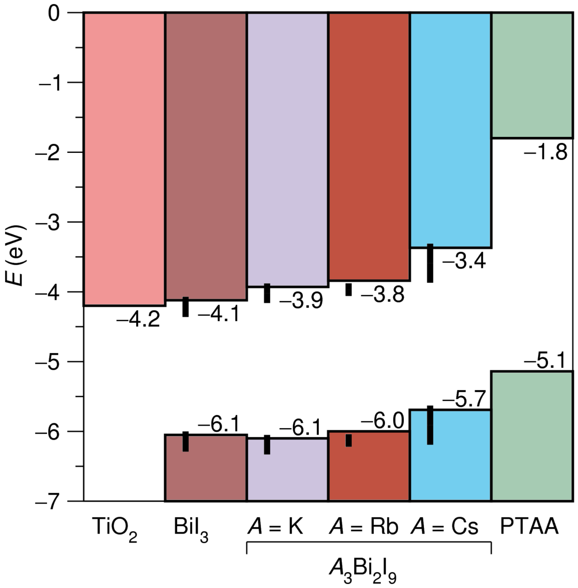

Figure 7: Band positions derived from DFT calculations (PBE+SOC), compared to experimental values (indicated by vertical bars as a range for the UPS experiments carried out here) for $A_3Bi_2I_9$ (A = K, Rb, Cs) and BiI_3. For added comparison, the experimental band positions of PTAA[70] and the calculated CBM of anatase TiO_2[56] are also displayed.

The resulting calculated band positions are shown in Figure 7 for the ternaries $A_3Bi_2I_9$ (A = K, Rb, Cs) in comparison to BiI_3. Experimentally determined VBM positions and band gaps are represented as bars indicating a range of UPS measurements on different samples, the positions of the conduction band minima (CBM) were derived as CBM =

VBM + E_g. In addition, the band positions of each of a commonly used electron and hole transport material for heavy metal halide photovoltaic devices, anatase TiO_2 and Polyarylamide PTAA,[71] are included. Here, taking into account the broad spectral absorption in the optical range, we suggest using the bismuth halides as solar cell absorber layer instead of as previously reported as hole transport layer.[13] The calculated E_g and VBM values are listed in Table 4. The agreement of the calculated values to the experimental data ranges is remarkable, suggesting that our relatively fast method of deriving absolute band positions from slab calculations only for a relatively simple reference compound and only needing advanced level (HSE+SOC) single unit cell DOS can be an excellent screening tool. The calculated band gaps for the ternary iodides increase from 2.2 eV to 2.3 eV with increasing counter cation size. This trend is not in agreement with the experimentally determined gaps in this and previous work[33] which might be due to the fact that the Cs salt unit cell volume is relatively more overestimated during the DFT structure optimization compared to the lighter alkali metal homologues. The VBM levels for the 2D layered K and Rb bismuth iodides around -6.0 eV are very similar to the layered BiI_3, and thus the nature and size of the counter cation (or even its absence) does not seem to have be relevant to the VBM position as long as the dimensionality of the Bi-I-units remains the same. In comparison, the 0D $Cs_3Bi_2I_9$ exhibits a shallower level. The same trend was reported for the series of hybrid lead iodides ranging from the 3D perovskite $CH_3NH_3PbI_3$ to layered derivatives of decreasing perovskite slab thickness.[72] For the layered antimony homologue $Cs_3Sb_2I_9$, the ionization potential was also reported to be 5.7 eV.[29] Potentially this is due to competing effects: increased anion dimensionality deepening the VBM and the lighter Sb central cation raising the VBM again to the same level as for $Cs_3Bi_2I_9$. For the heavier homologue, Bi, with its more contracted s-like states, we expect less covalent interaction and thus less band dispersion in the region of the antibonding M(s)-I(p) interaction at the top of the valence band. However, the VBM levels of the complex bismuth iodides are considerably deeper than the related lead iodides (e.g. -5.4 eV for $CH_3NH_3PbI_3$[73]). This creates a new challenges for the choice of hole transport layers for photovoltaic devices: the application of the commonly used polymers with VBMs not much below 5 eV would limit the open circuit voltage, and thus the power conversion efficiency.

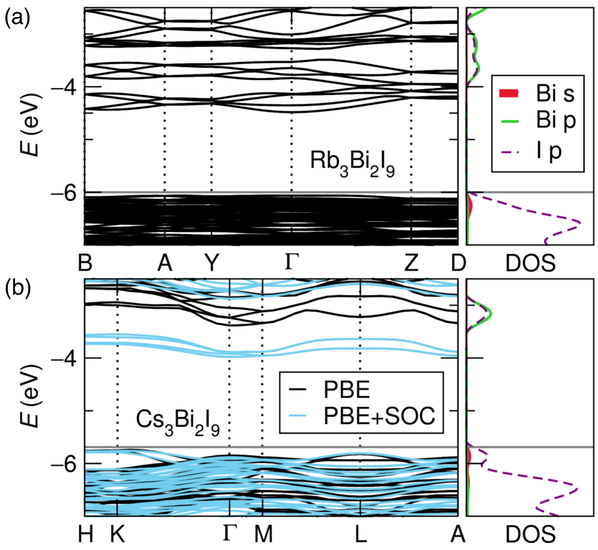

Figure 8: Band structure and partial density of states (DOS, HSE+SOC) of (a) $\mathrm{Rb_3Bi_2I_9}$ ($P2_1/c$) and (b) $\mathrm{Cs_3Bi_2I_9}$ ($P6_3/mmc$). The position of the valence band maximum (VBM, horizontal line) was offset based on slab calculations of $\mathrm{BiI_3}$. The calculated band gaps (HSE+SOC) are direct at Γ for $A_3\mathrm{Bi_2I_9}$ (A = K, Rb) and indirect between $0.75\overline{\Gamma\mathrm{K}}$ in the valence band and Γ in the conduction band for $\mathrm{Cs_3Bi_2I_9}$.

For photovoltaic device construction, in addition to efficient solar light absorption and well-aligned transport band positions of the components, long charge carrier diffusion lengths are essential. In electronic band structures the curvature of the bands is correlated with charge carrier effective mass and thus pronounced band dispersions can be indicative of high mobility.[74] Additionally, the band bonding character of heavy metal halides has been correlated with defect-tolerance.[34] As the band structures of the isotypic layered $\mathrm{K_3Bi_2I_9}$ and $\mathrm{Rb_3Bi_2I_9}$ phases are almost identical around the band gap, only the data for the Rb salt is included in Figure 8a for clarity. We will focus mainly on the comparison of the 2D vs 0D structure types for the examples of the Rb and Cs salt for the remainder of the discussion of computational results. For those layered salts, a direct band gap of 2.17 eV (K), or 2.16 eV (Rb) at Γ was obtained at HSE+SOC level of theory. The dispersion of the lowest conduction bands is moderate, while the top valence bands are very flat, indicating smaller effective masses for electrons compared to holes. For $Cs_3Bi_2I_9$ (Figure 8b), the valence band dispersion is larger while still relatively small compared to the related 3D halide perovskites.[75] From our HSE+SOC calculations, the band gap of $Cs_3Bi_2I_9$ (2.32 eV) is located between $0.75\overline{\Gamma \mathrm{K}}$ in the valence band and Γ in the conduction band. From the comparison of the relatively flat band structures of the $A_3Bi_2I_9$ phases to highly dispersive ones of the 3D perovskites,[56,75] one could conclude that the M-I-M bond angles rather than the connectivity mode have a strong influence on the band curvature and thus effective carrier masses and mobility: In the 3D perovskite structures, the near 180° M-I-M angles connecting the octahedra facilitate a better band overlap resulting in a better carrier transport through the metal halide lattice than in the defect-perovskites $A_3Bi_2I_9$ with Bi-I-Bi angles of around 150°. The $Cs_3Bi_2I_9$ and BiI_3 structures, with their shorter Bi-Bi distances due to face or edge-sharing octahedra, respectively, naturally exhibit even smaller Bi-I-Bi bond angles. The partial density of states plots show that the excitation across the gap occurs for all phases mainly from occupied I p states with a small contribution of Bi s states into empty Bi p + I p states.

In the homologous alkali antimony halides such as $Cs_3Sb_2I_9$[29] and in the isoelectronic tetrel halide perovskites[56,76–78] the optical transition involves the same corresponding states and these materials' unique optoelectronic properties have been attributed in part to the effect of the ns^2 metal ions. For $CH_3NH_3PbI_3$, the strong p-character of the valence and the conduction band around the gap have been reported to lead to a high joint density of states, resulting in an unusually large optical absorption coefficient.[77] The combination of a direct band gap and p-p optical transitions in the 2D layered $A_3Bi_2I_9$ phases makes them very promising for next generation optoelectronics.

As discussed above, there are no obvious signs of stereochemical activity of the Bi^{3+} 6s lone pair in the studied $A_3Bi_2I_9$ structures. However, those phases are prone to undergo structural phase transitions as reported for $Cs_3Bi_2I_9$,[24–26] which could be potentially lone-

Table 5: Dielectric properties of $A_3Bi_2I_9$ salts including the high-frequency dielectric tensors (ϵ_{ij}^{∞}) and Born effective charge tensors (Z^*; $|e|$) on Bi^{3+}.

Phase	Method	ϵ_{xx}^{∞}	ϵ_{yy}^{∞}	ϵ_{zz}^{∞}	Z_{xx}^*	Z_{yy}^*	Z_{zz}^*
$Rb_3Bi_2I_9$	PBE	19.3	22.3	65.5	4.4	4.3	4.9
$Cs_3Bi_2I_9$	PBE	5.5		4.2	2.8	-	3.4
$Cs_3Bi_2I_9$	PBE+SOC	7.6		5.7	3.9	-	3.9

pair-driven. Calculated Born effective charge tensors on the lone-pair-bearing atom and the dielectric constants have been used previously used to probe the lone-pair activity and proximal structural instabilities in heavy metal phases.[56,76,79–83] Interestingly, anomalously large Born tensors have also been suggested to indicate effective screening of defects and impurities which would otherwise be strong charge carrier traps, contributing to good carrier transport properties in heavy metal halides.[76,80] The calculated Born tensors Z^* and high-frequency (ion-clamped) dielectric tensors ϵ_{ij}^{∞} for the 0D and 2D examples of $A_3Bi_2I_9$ are listed in Table 5. Comparing the two computational schemes (PBE vs. PBE+SOC) used for $Cs_3Bi_2I_9$, it can be observed that including SOC increases the magnitude of ϵ_{ij}^{∞} as well as Z^* by ≈15%-40% due to reorganization of the band structure. However, it is clear that elevated Z^* values can be identified without applying the much more time-consuming SOC calculations. While for $Cs_3Bi_2I_9$, the Born charges are not significantly higher than the nominal charge, the layered defect-perovskite phase $Rb_3Bi_2I_9$ exhibits Z^* values of 4.3 to 4.9 on Bi^{3+}. Correspondingly, for BiI_3, a large in-plane Born charge on Bi^{3+} has been calculated and it was suggested to be correlated with the substantial covalent interaction between Bi 6p and halogen p states.[79] From this one can conclude that the 2D phases might be more defect-tolerant than the 0D bismuth halide phases. However, the applicability of Cs_2SnI_6 which contains isolated SnI_6^{2-} octahedra as a photovoltaic hole transport layer,[84] enforces our point that the structural influences on the optoelectronic properties of heavy main group metal halides are complex and even the phases with low dimensional bismuth halide units hold the potential for interesting future applications.

4 Conclusion

In the search for promising materials for optoelectronic applications, we look for band gaps that are well-matched with the excitation spectrum, efficient light absorption, and facile carrier transport.[34] Here we have investigated complex bismuth iodides $A_3Bi_2I_9$ (A = K, Rb, Cs) both experimentally and computationally. New facile preparation routes from organic solvents and by mechanical mixing are presented and initial thin film fabrication procedures are reported. From our preliminary observations, the chemical stability seems to be greater than for the related lead halides. Crystal structures were redetermined by X-ray diffraction, as the basis for advancing structure-composition-property relationships. For the layered defect-perovskite $Rb_3Bi_2I_9$, we report an improved centrosymmetric structural model based on single-crystal diffraction and solid state NMR supported by DFT simulation of NMR parameters. The optical band gaps and absolute VBM positions were determined by UV-Vis and by ultraviolet photoemission spectroscopy, respectively. Band structures were calculated using the screened hybrid functional HSE, and including spin-orbit coupling for the band gaps, and slab-calculations for absolute band positions using the binary BiI_3 phase as a reference, that allowed other absolute band positions to be obtained. The excellent agreement between experimental and calculated values suggest that the methods employed here are a powerful tool for the rapid screening of semiconductors and the rational design of optoelectronic devices.

Key findings that resulted for the compounds studied are that the band gaps are around 2 eV and are rather insensitive to the counter cation and structure type. In addition, the VBM levels are significantly lower than for the widely used lead halide perovskite photovoltaics. Thus, for potential application in solar cells, in addition to the optimization of the film formation, a careful choice of the contacting hole transport materials will be necessary to match the band positions and enable high open circuit voltages. From the calculated band structures, the band gaps of the layered K and Rb salts are direct, while $Cs_3Bi_2I_9$ has an indirect gap. Direct gaps coupled with the high density of states with a strong p-character across the gap, as observed for the studied phases, are quite promising for effective light absorption. For the three phases, the band dispersion of the conduction and valence bands around the gap is moderate to small compared to the related perovskite halides, possibly as a result of the different relative arrangement of the BiI_6 octahedra. The calculated Born effective charges on Bi^{3+} are significantly elevated only for the layered $A_3Bi_2I_9$ and not for the 0D $Cs_3Bi_2I_9$. High Born effective charges are indicative of more efficient dielectric defect screening and thus potentially, better carrier mobility. Given the solution-processability and the range of similar optoelectronic properties paired with a much lower toxicity compared to the lead halide perovskites, the structurally rich class of complex bismuth halides is a new promising class of materials for optoelectronic application.

Supporting Information Available

Relevant group-subgroup relationships, crystallographic data including bond distances, single-pulse ^{87}Rb NMR spectra displaying peak deconvolution, UPS spectra of $Rb_3Bi_2I_9$ and $Cs_3Bi_2I_9$, and densities of state (DOS) for the title compounds from DFT calculations, explaining the use of deep s states of Bi to carry out relative band alignments. This material is available free of charge via the Internet at `http://pubs.acs.org/`.

Acknowledgement

This work was supported by the U.S. Department of Energy, Office of Science, Basice Energy Sciences under award number DE-SC-0012541. We thank Prof. Jakoah Brgoch for fruitful discussions. A.J.L gratefully acknowledges support of Swiss National Science Foundation fellowship number PBSKP2-145825. The research involved the use of shared experimental facilities of the Materials Research Laboratory and the Center for Scientific Computing at UCSB supported by the MRSEC Program of the National Science Foundation under Award No. DMR 1121053 and NSF CNS-0960316, and additional computational facilities provided by ACENET, the regional high performance computing consortium for universities in Atlantic Canada, funded by the Canada Foundation for Innovation (CFI), the Atlantic Canada Opportunities Agency (ACOA), and the provinces of Newfoundland and Labrador, Nova Scotia, and New Brunswick. Use of data from beamline 11-BM at the Advanced Photon Source is supported by the Department of Energy, Office of Science, Office of Basic Energy Sciences, under Contract No. DE-AC02-06CH11357.

References

(1) Stoumpos, C. C.; Frazer, L.; Clark, D. J.; Kim, Y. S.; Rhim, S. H.; Freeman, A. J.; Ketterson, J. B.; Jang, J. I.; Kanatzidis, M. G. Hybrid Germanium Iodide Perovskite Semiconductors: Active Lone Pairs, Structural Distortions, Direct and Indirect Energy Gaps, and Strong Nonlinear Optical Properties. *J. Am. Chem. Soc.* **2015**, *137*, 6804–6819.

(2) Hao, F.; Stoumpos, C. C.; Cao, D. H.; Chang, R. P. H.; Kanatzidis, M. G. Lead-Free Solid-State Organic-Inorganic Halide Perovskite Solar Cells. *Nat. Photonics* **2014**, *8*, 489–494.

(3) Knutson, J. L.; Martin, J. D.; Mitzi, D. B. Tuning the Band Gap in Hybrid Tin Iodide Perovskite Semiconductors Using Structural Templating. *Inorg. Chem.* **2005**, *44*, 4699–4705.

(4) Miyasaka, T. Organo-Lead Halide Perovskite: Rare Functions in Photovoltaics and Optoelectronics. *Chem. Lett.* **2015**, *44*, 720–729.

(5) Park, N.-G. Perovskite Solar Cells: An Emerging Photovoltaic Technology. *Mater. Today* **2015**, *18*, 65–72.

(6) Nason, D.; Keller, L. The Growth and Crystallography of Bismuth Tri-Iodide Crystals Grown by Vapor Transport. *J. Cryst. Growth* **1995**, *156*, 221–226.

(7) Lintereur, A. T.; Qiu, W.; Nino, J. C.; Baciak, J. Characterization of Bismuth Tri-Iodide Single Crystals for Wide Band-Gap Semiconductor Radiation Detectors. *Nucl. Instrum. Methods Phys. Res. A* **2011**, *652*, 166–169.

(8) Han, H.; Hong, M.; Gokhale, S. S.; Sinnott, S. B.; Jordan, K.; Baciak, J. E.; Nino, J. C. Defect Engineering of BiI_3 Single Crystals: Enhanced Electrical and Radiation Perfor-

mance for Room Temperature Gamma-Ray Detection. *J. Phys. Chem. C* **2014**, *118*, 3244–3250.

(9) Gokhale, S. S.; Han, H.; Baciak, J. E.; Nino, J. C.; Jordan, K. A. Growth, Fabrication, and Testing of Bismuth Tri-Iodide Semiconductor Radiation Detectors. *Radiat. Meas.* **2015**, *74*, 47–52.

(10) Cuña, A.; Aguiar, I.; Gancharov, A.; Pérez, M.; Fornaro, L. Correlation Between Growth Orientation and Growth Temperature for Bismuth Tri-Iodide Films. *Crys. Res. Technol.* **2004**, *39*, 899–905.

(11) Cuña, A.; Noguera, A.; Saucedo, E.; Fornaro, L. Growth of Bismuth Tri-Iodide Platelets by the Physical Vapor Deposition Method. *Crys. Res. Technol.* **2004**, *39*, 912–919.

(12) Aguiar, I.; Kröger, S.; Fornaro, L. Bismuth Tri-Iodide Polycrystalline Films for X-Ray Direct and Digital Imagers. *Nucl. Instrum. Methods Phys. Res., Sect. A* **2009**, *610*, 332–334.

(13) Boopathi, K. M.; Raman, S.; Mohanraman, R.; Chou, F.-C.; Chen, Y.-Y.; Lee, C.-H.; Chang, F.-C.; Chu, C.-W. Solution-Processable Bismuth Iodide Nanosheets as Hole Transport Layers for Organic Solar Cells. *Sol. Energy Mater. Sol. Cells* **2014**, *121*, 35–41.

(14) Lehner, A. J.; Wang, H.; Fabini, D.; Liman, C. D.; Hébert, C.; Perry, E. E.; Wang, M.; Bazan, G. C.; Chabinyc, M. L.; Seshadri, R. Electronic structure and photovoltaic application of BiI_3. *Appl. Phys. Lett.* **2015**, *107*, 131109.

(15) Wu, L.-M.; Wu, X.-T.; Chen, L. Structural Overview and Structure-Property Relationships of Iodoplumbate and Iodobismuthate. *Coord. Chem. Rev.* **2009**, *253*, 2787–2804.

(16) Mitzi, D. B. Organic-Inorganic Perovskites Containing Trivalent Metal Halide Layers: The Templating Influence of the Organic Cation Layer. *Inorg. Chem.* **2000**, *39*, 6107–6113.

(17) Kodzasa, T.; Ushijima, H.; Matsuda, H.; Kamata, T. Preparation of Thin Film of Layer Structured Bismuth Iodide with a Long Chain Alkylammonium and its Nonlinear Optical Property. *Mol. Cryst. Liq. Cryst. Sci. Technol. A* **2000**, *343*, 71–75.

(18) Mitzi, D. B.; Brock, P. Structure and Optical Properties of Several Organic-Inorganic Hybrids Containing Corner-Sharing Chains of Bismuth Iodide Octahedra. *Inorg. Chem.* **2001**, *40*, 2096–2104.

(19) Dammak, H.; Yangui, A.; Triki, S.; Abid, Y.; Feki, H. Structural Characterization, Vibrational, Optical Properties and DFT Investigation of a New Luminescent OrganicInorganic Material: $(C_6H_{14}N)_3Bi_2I_9$. *J. Lumin.* **2015**, *161*, 214–220.

(20) Sidey, V.; Voroshilov, Y.; Kun, S.; Peresh, E. Crystal Growth and X-Ray Structure Determination of $Rb_3Bi_2I_9$. *J. Alloys Compd.* **2000**, *296*, 53–58.

(21) Preitschaft, C. Ternäre und quaternäre Materialien mit Komplexen Thio-, Selenido- und Halogenid-Anionen. Ph.D. thesis, Universität Regensburg, 2004.

(22) Lindquist, O. The Crystal Structure of Caesium Bismuth Iodide, $Cs_3Bi_2I_9$. *Acta Chem. Scand.* **1968**, *22*, 2943–2952.

(23) Aleksandrov, I. P.; Bovina, A. F.; Ageev, O. A.; Sukhovskii, A. A. Incommensurate Phase in the Layered Hexagonal Crystal $Cs_3Bi_2I_9$. *Phys. Solid State* **1997**, *39*, 991–994.

(24) Melnikova, S. V.; Zaitsev, A. I. Ferroelectric Phase Transition in $Cs_3Bi_2I_9$. *Phys. Solid State* **1997**, *39*, 1652–1654.

(25) Jorio, A.; Currat, R.; Myles, D. A. A.; McIntyre, G. J.; Aleksandrova, I. P.; Kiat, J. M.; Saint-Grégoire, P. Ferroelastic Phase Transition in $Cs_3Bi_2I_9$: A Neutron Diffraction Study. *Phys. Rev. B* **2000**, *61*, 3857–3862.

(26) Arakcheeva, A.; Chapuis, G.; Meyer, M. The LT phase of $Cs_3Bi_2I_9$. *Z. Kristallogr.* **2001**, *216*, 199–205.

(27) Lazarini, F. Caesium enneabromodibismuthate(III). *Acta Crystallogr. B* **1977**, *33*, 2961–2964.

(28) Aleksandrov, K. S.; Beznosikov, V. V. Hierarchies of Perovskite-Like Crystals (Review). *Phys. Solid State* **1997**, *39*, 695–715.

(29) Saparov, B.; Hong, F.; Sun, J.-P.; Duan, H.-S.; Meng, W.; Cameron, S.; Hill, I. G.; Yan, Y.; Mitzi, D. B. Thin-Film Preparation and Characterization of $Cs_3Sb_2I_9$: A Lead-Free Layered Perovskite Semiconductor. *Chem. Mater.* **2015**, 150709082114007.

(30) Zamkov, A. V.; Zaitsev, A. I.; Parshikov, S. A.; Sysoev, A. M. Acoustooptic Properties of $Cs_3Bi_2I_9$ Crystals. *Inorg. Mater.* **2001**, *37*, 82–83.

(31) Motsnyi, F. V.; Peresh, E. Y.; Smolanka, O. M. Nontraditional Temperature Shift of the Fundamental Absorption Edge for Layered Substances and the Ferroelastic Phase Transition in $Cs_3Bi_2I_9$. *Solid State Commun.* **2004**, *131*, 469–471.

(32) Peresh, E. Y.; Sidei, V. I.; Zubaka, O. V.; Stercho, I. P. $K_2(Rb_2,Cs_2,Tl_2)TeBr_6(I_6)$ and $Rb_3(Cs_3)Sb_2(Bi_2)Br_9(I_9)$ Perovskite Compounds. *Inorg. Mater.* **2011**, *47*, 208–212.

(33) Peresh, E. Y.; Sidei, V. I.; Gaborets, N. I.; Zubaka, O. V.; Stercho, I. P.; Barchii, I. E. Influence of the Average Atomic Number of the A_2TeC_6 and $A_3B_2C_9$ (A = K, Rb, Cs, Tl(I); B = Sb, Bi; C = Br, I) Compounds on Their Melting Point and Band Gap. *Inorg. Mater.* **2014**, *50*, 111–116.

(34) Brandt, R. E.; Stevanović, V.; Ginley, D. S.; Buonassisi, T. Identifying Defect-Tolerant Semiconductors with High Minority-Carrier Lifetimes: Beyond Hybrid Lead Halide Perovskites. *MRS Commun.* **2015**, *5*, 265–275.

(35) Coelho, A. A. TOPAS-Academic V5. 2013.

(36) SAINT: Data Reduction and Frame Integration Program for the CCD Area-Detector System. Bruker Analytical X-ray Systems, Inc. Madison WI, USA., 1999.

(37) SADABS: Area-Detector Absorption Correction. Siemens Industrial Automation Inc. Madison WI, USA, 1996.

(38) Sheldrick, G. M. SHELXS-97 - Program for the Solution of Crystal Structures. University of Göttingen, Germany, 1997.

(39) Sheldrick, G. M. A Short History of SHELX. *Acta Crystallogr. A* **2008**, *64*, 112–122.

(40) Momma, K.; Izumi, F. VESTA3 for Three-Dimensional Visualization of Crystal, Volumetric and Morphology Data. *J. Appl. Crystallogr.* **2011**, *44*, 1272–1276.

(41) Burnett, M. N.; Johnson, C. K. ORTEP-III: Oak Ridge Thermal Ellipsoid Plot Program for Crystal Structure Illustrations. 1996.

(42) Baltisberger, J. H.; Gann, S. L.; Wooten, E. W.; Chang, T. H.; Mueller, K. T.; Pines, A. Rb-87 Dynamic Angle spinning NMR Spectroscopy of Inorganic Rb Salts. *J. Am. Chem. Soc.* **1992**, *114*, 7489–7493.

(43) Tauc, J.; Grigorovici, R.; Vancu, A. Optical Properties and Electronic Structure of Amorphous Germanium. *Phys. Stat. Sol.* **1966**, *15*, 627–637.

(44) Tauc, J. Optical Properties and Electronic Structure of Amorphous Ge and Si. *Mater. Res. Bull.* **1968**, *3*, 37–46.

(45) Kresse, G.; Hafner, J. Ab Initio Molecular Dynamics for Liquid Metals. *Phys. Rev. B* **1993**, *47*, 558–561.

(46) Kresse, G.; Hafner, J. Ab Initio Molecular-Dynamics Simulation of the Liquid-Metal-Amorphous-Semiconductor Transition in Germanium. *Phys. Rev. B* **1994**, *49*, 14251–14269.

(47) Kresse, G.; Furthmüller, J. Efficiency of Ab-Initio Total Energy Calculations for Metals and Semiconductors Using a Plane-Wave Basis Set. *Comput. Mat. Sci.* **1996**, *6*, 15–50.

(48) Kresse, G.; Furthmüller, J. Efficient Iterative Schemes for ab Initio Total-Energy Calculations Using a Plane-Wave Basis Set. *Phys. Rev. B* **1996**, *54*, 11169–11186.

(49) Blöchl, P. E. Projector Augmented-Wave Method. *Phys. Rev. B* **1994**, *50*, 17953–17979.

(50) Kresse, G.; Joubert, D. From Ultrasoft Pseudopotentials to the Projector Augmented-Wave Method. *Phys. Rev. B* **1999**, *59*, 1758–1775.

(51) Aroyo, M. I.; Orobengoa, D.; de la Flor, G.; Perez-Mato, J. M.; Wondratschek, H. Brillouin-Zone Databases on the Bilbao Crystallographic Server. *Acta Crystallogr. A* **2014**, *70*, 126–137.

(52) Perdew, J. P.; Burke, K.; Ernzerhof, M. Generalized Gradient Approximation Made Simple. *Phys. Rev. Lett.* **1996**, *77*, 3865–3868.

(53) Heyd, J.; Scuseria, G. E.; Ernzerhof, M. Hybrid Functionals Based on a Screened Coulomb Potential. *J. Chem. Phys.* **2003**, *118*, 8207–8215.

(54) Heyd, J.; Scuseria, G. E.; Ernzerhof, M. Erratum: Hybrid Functionals Based on a Screened Coulomb Potential. *J. Chem. Phys.* **2006**, *124*, 219906.

(55) Van de Walle, C. G.; Martin, R. M. Theoretical Calculations of Heterojunction Discontinuities in the Si/Ge System. *Phys. Rev. B* **1986**, *34*, 5621–5634.

(56) Brgoch, J.; Lehner, A. J.; Chabinyc, M.; Seshadri, R. Ab Initio Calculations of Band Gaps and Absolute Band Positions of Polymorphs of $RbPbI_3$ and $CsPbI_3$: Implications for Main-Group Halide Perovskite Photovoltaics. *J. Phys. Chem. C* **2014**, *118*, 27721–27727.

(57) Giannozzi, P.; Baroni, S.; Bonini, N.; Calandra, M.; Car, R.; Cavazzoni, C.; Ceresoli, D.; Chiarotti, G. L.; Cococcioni, M.; Dabo, I.; Dal Corso, A.; de Gironcoli, S.; Fabris, S.; Fratesi, G.; Gebauer, R.; Gerstmann, U.; Gougoussis, C.; Kokalj, A.; Lazzeri, M.; Martin-Samos, L.; Marzari, N.; Mauri, F.; Mazzarello, R.; Paolini, S.; Pasquarello, A.; Paulatto, L.; Sbraccia, C.; Scandolo, S.; Sclauzero, G.; Seitsonen, A. P.; Smogunov, A.; Umari, P.; Wentzcovitch, R. M. QUANTUM ESPRESSO: A Modular and Open-Source Software Project for Quantum Simulations of Materials. *J. Phys.: Condens. Matter* **2009**, *21*, 395502–1–395502–19.

(58) Pickard, C. J.; Mauri, F. All-Electron Magnetic Response with Pseudopotentials: NMR Chemical Shifts. *Phys. Rev. B* **2001**, *63*, 245101–1–245101–13.

(59) Yates, J. R.; Pickard, C. J.; Mauri, F. Calculation of NMR Chemical Shifts for Extended Systems Using Ultrasoft Pseudopotentials. *Phys. Rev. B* **2007**, *76*, 024401–1–024401–11.

(60) Profeta, M.; Mauri, F.; Pickard, C. J. Accurate First Principles Prediction of ^{17}O NMR Parameters in SiO_2: Assignment of the Zeolite Ferrierite Spectrum. *J. Am. Chem. Soc.* **2003**, *125*, 541–548.

(61) Jollet, F.; Torrent, M.; Holzwarth, N. Generation of Projector Augmented-Wave Atomic Data: A 71 Element Validated Table in the XML Format. *Comput. Phys. Comm.* **2014**, *185*, 1246–1254.

(62) Holzwarth, N.; Tackett, A.; Matthews, G. A Projector Augmented Wave (PAW) Code

for Electronic Structure Calculations, Part I: Atompaw for Generating Atom-Centered Functions. *Comput. Phys. Comm.* **2001**, *135*, 329–347.

(63) Peresh, E. Y.; Lazarev, V. B.; Kun, S. V.; Barchii, I. E.; Kun, A. V.; Sidei, V. I. Mixed Halides $A_3B_2C_9$ (A = Rb, Cs; B = Sb, Bi; C = Br, I) and Their Solid Solutions. *Inorg. Mater.* **1997**, *33*, 362–365.

(64) Ruck, M. Darstellung und Kristallstruktur von Fehlordnungsfreiem Bismuttriiodid. *Z. Kristallogr.* **1995**, *210*, 650–655.

(65) Wessel, G. J.; Ijdo, D. J. W. The Crystal Structure of $Cs_3Cr_2Cl_9$. *Acta Crystallogr.* **1957**, *10*, 466–468.

(66) Wosylus, A.; Schwarz, U.; Ruck, M. Die Kristallstruktur von $Tl_3Bi_2I_9$: Eine komplexe Ausdünnungs- und Verzerrungsvariante des Perowskit-Typs. *Z. Anorg. Allg. Chem.* **2005**, *631*, 1055–1059.

(67) Guthrie, D. H.; Meyer, G.; Corbett, J. D. Metal-Metal Repulsion and Bonding in Confacial Bioctahedra. The Crystal Structures of Cesium Yttrium Iodide ($Cs_3Y_2I_9$) and Cesium Zirconium Iodide ($Cs_3Zr_2I_9$) and Comparison with Related Phases. *Inorg. Chem.* **1981**, *20*, 1192–1196.

(68) Shannon, R. D. Revised Effective Ionic Radii and Systematic Studies of Interatomic Distances in Halides and Chalcogenides. *Acta Crystallogr. A* **1976**, *32*, 751–767.

(69) De Wolf, S.; Holovsky, J.; Moon, S.-J.; Löper, P.; Niesen, B.; Ledinsky, M.; Haug, F.-J.; Yum, J.-H.; Ballif, C. Organometallic Halide Perovskites: Sharp Optical Absorption Edge and its Relation to Photovoltaic Performance. *J. Phys. Chem. Lett.* **2014**, *5*, 1035–1039.

(70) Schols, S. *Device architecture and Materials for Organic Light-emitting Devices: Target-*

ing High Current Densities and Control of the Triplet Concentration; Springer Science & Business Media, 2011.

(71) Veres, J.; Ogier, S.; Leeming, S.; Brown, B.; Cupertino, D. Air Stable, Amorphous Organic Films and Their Applications to Solution Processable Flexible Electronics. *Mater. Res. Soc. Symp. Proc.* **2001**, *708*, BB8.7.

(72) Cao, D. H.; Stoumpos, C. C.; Farha, O. K.; Hupp, J. T.; Kanatzidis, M. G. 2D Homologous Perovskites as Light-Absorbing Materials for Solar Cell Applications. *J. Am. Chem. Soc.* **2015**, *137*, 7843–7850.

(73) Schulz, P.; Edri, E.; Kirmayer, S.; Hodes, G.; Cahen, D.; Kahn, A. Interface Energetics in Organo-Metal Halide Perovskite-Based Photovoltaic Cells. *Energy Environ. Sci.* **2014**, 1377–1381.

(74) Ashcroft, N. W.; Mermin, N. D. *Solid State Physics*; Brooks/Cole: New York, 1976.

(75) Even, J.; Pedesseau, L.; Jancu, J.-M.; Katan, C. Importance of Spin-Orbit Coupling in Hybrid Organic/Inorganic Perovskites for Photovoltaic Applications. *J. Phys. Chem. Lett.* **2013**, *4*, 2999–3005.

(76) Du, M. H. Efficient Carrier Transport in Halide Perovskites: Theoretical Perspectives. *J. Mater. Chem.* **2014**, *2*, 9091–9098.

(77) Yin, W. J.; Shi, T.; Yan, Y. Unique Properties of Halide Perovskites as Possible Origins of the Superior Solar Cell Performance. *Adv. Mater.* **2014**, *26*, 4653–4658.

(78) Walsh, A. Principles of Chemical Bonding and Band Gap Engineering in Hybrid Organic-Inorganic Halide Perovskites. *J. Phys. Chem. C* **2015**, *119*, 5755–5760.

(79) Singh, D. J. Structure and Optical Properties of High Light Output Halide Scintillators. *Phys. Rev. B* **2010**, *82*, 155145–1–155145–10.

(80) Du, M.-H.; Singh, D. J. Enhanced Born Charge and Proximity to Ferroelectricity in Thallium Halides. *Phys. Rev. B* **2010**, *81*, 144114–1–144114–20.

(81) Miao, M.; Brgoch, J.; Krishnapriyan, A.; Goldman, A.; Kurzman, J. A.; Seshadri, R. On the Stereochemical Inertness of the Auride Lone Pair: Ab Initio Studies of AAu (A = K, Rb, Cs). *Inorg. Chem.* **2013**, *52*, 8183–8189.

(82) Huang, L.-Y.; Lambrecht, W. R. L. Electronic Band Structure, Phonons, and Exciton Binding Energies of Halide Perovskites $CsSnCl_3$, $CsSnBr_3$, and $CsSnI_3$. *Phys. Rev. B* **2013**, *88*, 165203–1–165203–12.

(83) Devidas, T. R.; Chandra Shekar, N. V.; Sundar, C. S.; Chithaiah, P.; Sorb, Y. a.; Bhadram, V. S.; Chandrabhas, N.; Pal, K.; Waghmare, U. V.; Rao, C. N. R. Pressure-Induced Structural Changes and Insulator-Metal Transition in Layered Bismuth Triiodide, BiI_3: A Combined Experimental and Theoretical Study. *J. Phys.: Condens. Matter* **2014**, *26*, 275502–1–275502–9.

(84) Lee, B.; Stoumpos, C. C.; Zhou, N.; Hao, F.; Malliakas, C.; Yeh, C.-Y.; Marks, T. J.; Kanatzidis, M. G.; Chang, R. P. H. Air-Stable Molecular Semiconducting Iodosalts for Solar Cell Applications: Cs_2SnI_6 as a Hole Conductor. *J. Am. Chem. Soc.* **2014**, *136*, 15379–15385.

Graphical TOC Entry

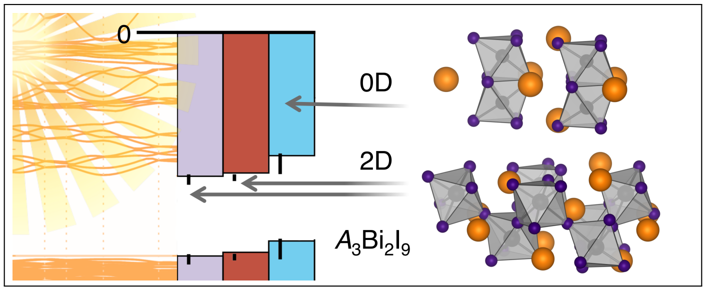

Supporting Information for: Crystal and Electronic Structures of Complex Bismuth Iodides $A_3Bi_2I_9$ (A = K, Rb, Cs) Related to Perovskite: Aiding the Rational Design of Photovoltaics

Anna J. Lehner,[*,†,‡] Douglas H. Fabini,[¶,‡] Hayden A. Evans,[§,‡]

Claire-Alice Hébert,[‖] Sara R. Smock,[§] Jerry Hu,[‡] Hengbin Wang,[†]

Josef W. Zwanziger,[⊥,#] Michael L. Chabinyc,[†,¶,‡] and Ram Seshadri[†,‡,¶,§]

†Mitsubishi Chemical Center for Advanced Materials

‡Materials Research Laboratory

¶Materials Department

§Department of Chemistry and Biochemistry

‖College of Creative Studies, University of California, Santa Barbara CA 93106, United States

⊥Department of Chemistry, Dalhousie University, Halifax, NS B3H 4R2, Canada

#Institute for Research in Materials, Dalhousie University, Halifax, NS B3H 4R2, Canada

E-mail: alehner@mrl.ucsb.edu

Supporting Information

$$\mathbb{A} = \left(\begin{array}{ccc|c} 1 & 0 & 0 & 0 \\ 0 & 1 & 0 & 1/4 \\ 0 & 0 & 1 & 0 \end{array}\right) \qquad \mathrm{A} = \left(\begin{array}{ccc} 0 & 0 & \bar{1} \\ 0 & 1 & 0 \\ 1 & 0 & \bar{1} \end{array}\right)$$

Figure S1: The group subgroup relation between $P2_1/c$ and Pc is characterized by an index t2 and the rotation-translation transformation matrix $\mathbb{A}$, which relates the coordinate system of the subgroup to that of the supergroup. Upon symmetry reduction from $P2_1/c$ to Pc, each atomic position, Wyckoff site $4e$, splits into two sites $2a$. The coordinate system of the space group $P2_1/n$ can be transformed to the setting $P2_1/c$ by the rotation matrix A.[1]

Table S1: Crystallographic parameters of A_3Bi$_2$I$_9$ (A = K, Rb, Cs) as determined by Rietveld refinement of PXRD data. Experimental densities derived from gas displacement pycnometry have been included for comparison.

Formula		$Rb_3Bi_2I_9$	$K_3Bi_2I_9$	$Cs_3Bi_2I_9$
Sample		⊢	powder	⊣
Structure type		⊢ $K_3Bi_2I_9$[2] ⊣		$Cs_3Cr_2Cl_9$[3]
Crystal system		⊢ monoclinic ⊣		hexagonal
Space group		⊢ $P2_1/n$ ⊣		$P6_3/mmc$
Unit cell (Å,°)				
	a	14.6968(1)	14.456(2)	8.4163(4)
	b	8.20241(6)	8.007(1)	
	c	20.9246(2)	20.801(4)	21.200(1)
	β	90.3957(3)	92.147(9)	
V (Å^3)		2522.38(3)	2406.1(7)	1300.5(1)
Z		4	4	2
Density (X-ray) (g/cm^3)		4.78	4.63	5.00
Density (Pycnom.) (g/cm^3)		4.82(2)	4.57(2)	5.09(1)
X-ray λ (Å)		0.45900	⊢ 1.54180 ⊣	
Diffractometer		11-BM APS	⊢ Philips X'Pert MPD ⊣	
T (K)		295	293	293
2Θ range (°)		2.8 to 45.5	8.0 to 70.0	6.0 to 65.0
No. free parameters		96	64	22
R_{wp}		0.0748	0.0531	0.0532
R_{exp}		0.0470	0.0305	0.0325
χ^2		1.59	1.74	1.64

Table S2: Selected interatomic distances (Å) in the crystal structure of $Rb_3Bi_2I_9$ ($P2_1/n$).

Sites		distance	CN	Sites		distance	CN
Rb1	- I8	3.645(2)		Bi1	- I6	2.9265(8)	
	- I1	3.700(2)			- I9	2.9357(9)	
	- I4	3.723(2)			- I3	2.9375(9)	
	- I2	3.769(2)			- I1	3.2028(9)	
	- I5	3.873(2)			- I8	3.2203(9)	
	- I5	3.938(2)			- I8	3.2257(9)	6
	- I9	3.939(2)					
	- I3	4.097(2)	8	Bi2	- I7	2.9221(9)	
					- I2	2.9265(8)	
Rb2	- I5	3.633(2)			- I4	2.9310(8)	
	- I6	3.708(2)			- I1	3.2015(9)	
	- I4	3.743(2)			- I5	3.2446(8)	
	- I9	3.755(2)			- I5	3.2541(9)	6
	- I3	3.925(2)					
	- I9	4.008(2)					
	- I2	4.062(2)					
	- I7	4.077(2)	8				
Rb3	- I3	3.698(2)					
	- I1	3.732(2)					
	- I7	3.769(2)					
	- I6	3.787(2)					
	- I2	3.964(2)					
	- I8	3.989(2)					
	- I8	4.006(2)					
	- I7	4.016(2)	8				

Table S3: Coefficients U_{ij} (Å^2) of the tensor of the anisotropic displacement parameters in the crystal structure of Rb$_3$Bi$_2$I$_9$ ($P2_1/n$) at 299 K.

Site	U_{11}	U_{22}	U_{33}	U_{12}	U_{13}	U_{23}
Rb1	0.0479(7)	0.0708(9)	0.068(1)	0.0069(7)	−0.0001(7)	−0.0055(7)
Rb2	0.082(1)	0.080(1)	0.054(1)	−0.0131(8)	−0.0102(8)	0.0129(8)
Rb3	0.0616(8)	0.080(1)	0.066(1)	0.0127(8)	−0.0051(7)	−0.0124(7)
Bi1	0.0275(2)	0.0316(2)	0.0236(2)	−0.0012(2)	0.0002(2)	−0.0014(2)
Bi2	0.0301(2)	0.0312(2)	0.0220(2)	0.0005(2)	−0.0009(2)	−0.0025(2)
I1	0.0452(4)	0.0758(6)	0.0593(6)	−0.0149(5)	−0.0306(4)	0.0124(4)
I2	0.0539(4)	0.0379(4)	0.0458(5)	−0.0087(3)	0.0047(4)	0.0120(3)
I3	0.0537(5)	0.0377(4)	0.0458(5)	−0.0123(3)	0.0048(4)	0.0043(3)
I4	0.0425(4)	0.0684(6)	0.0513(6)	0.0097(4)	−0.0204(4)	−0.0029(4)
I5	0.0538(4)	0.0390(4)	0.0371(5)	0.0098(3)	0.0084(3)	−0.0081(3)
I6	0.0383(4)	0.0699(6)	0.0488(6)	−0.0017(4)	−0.0182(4)	0.0054(4)
I7	0.0576(5)	0.0455(5)	0.0365(5)	−0.0102(3)	0.0078(4)	0.0049(4)
I8	0.0452(4)	0.0432(4)	0.0470(5)	−0.0153(4)	0.0121(4)	0.0035(3)
I9	0.0477(4)	0.0459(4)	0.0411(5)	0.0081(3)	0.0110(3)	−0.0092(4)

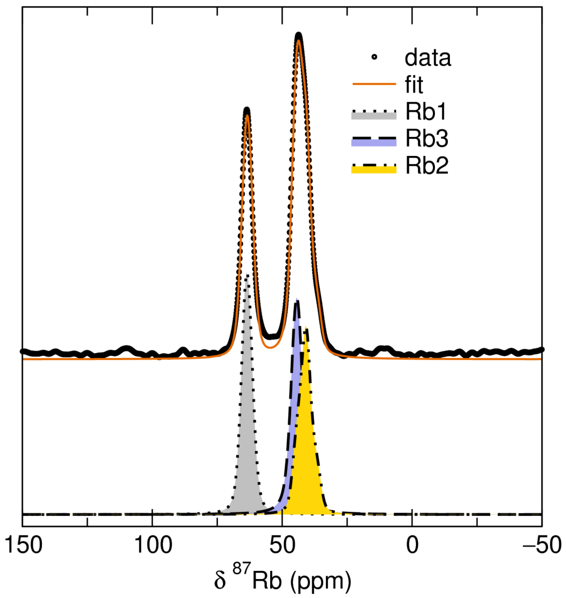

Figure S2: ^{87}Rb single pulse MAS NMR spectrum of $Rb_3Bi_2I_9$ recorded at 261.9 MHz. The spectrum was deconvoluted into three signals corresponding to the three Rb sites following the assignment established in the MQ-MAS studies. It is obvious how the observed signals are in stark contrast to what would be expected from our DFT calculations for the non-centrosymmetric structure published previously.[4]

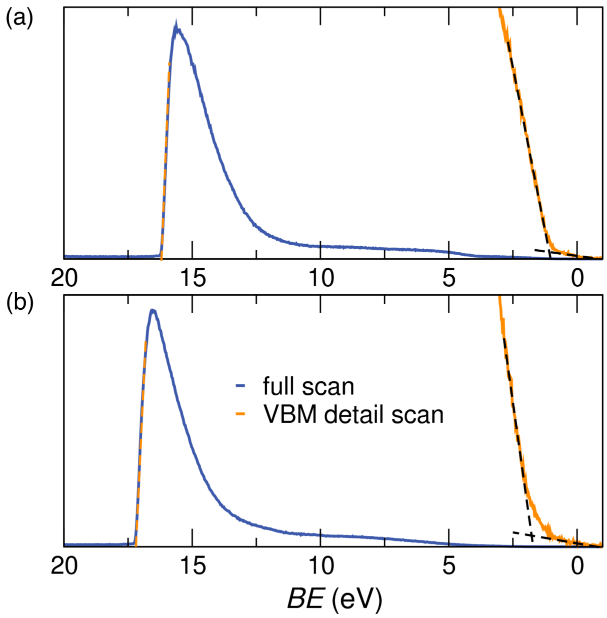

Figure S3: UPS spectra of (a) $Rb_3Bi_2I_9$ and (b) $Cs_3Bi_2I_9$. From UPS data, the position of the valence band maximum (VBM) was determined by subtracting the energy difference between both edges of the spectral feature from the excitation wavelength (He I lamp, 21.22 eV).

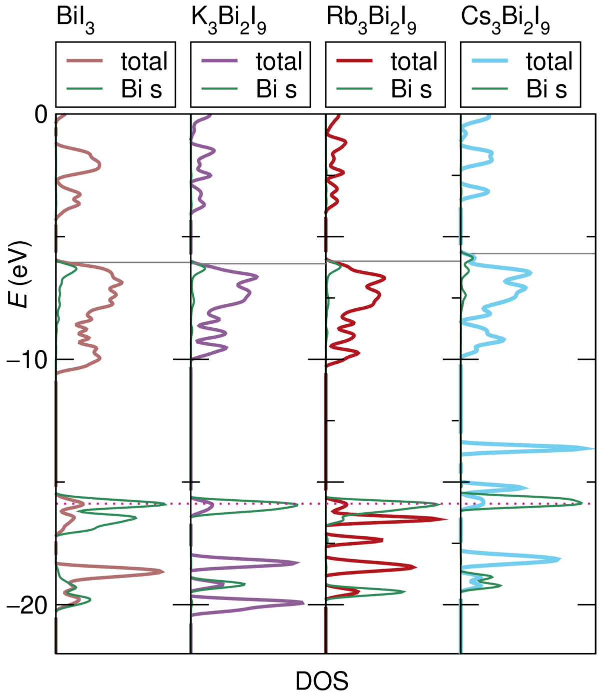

Figure S4: Absolute band position estimation for $A_3Bi_2I_9$ based on the calculated density of states (DOS, HSE+SOC) of a single unit cell. The s-like deep Bi states (horizontal dotted line) of the ternary iodides were aligned with the corresponding states in the DOS of BiI_3 which had been offset to an absolute scale using slab calculations.[5]

References

(1) Aroyo, M. I.; Perez-Mato, J. M.; Orobengoa, D.; Tasci, E.; de la Flor, G.; Kirov, A. Crystallography online: Bilbao Crystallographic Server. *Bulg. Chem. Commun.* **2011**, *43*, 183–197.

(2) Preitschaft, C. Ternäre und quaternäre Materialien mit Komplexen Thio-, Selenido- und Halogenid-Anionen. Ph.D. thesis, Universität Regensburg, 2004.

(3) Wessel, G. J.; Ijdo, D. J. W. The Crystal Structure of $Cs_3Cr_2Cl_9$. *Acta Crystallogr.* **1957**, *10*, 466–468.

(4) Sidey, V.; Voroshilov, Y.; Kun, S.; Peresh, E. Crystal Growth and X-Ray Structure Determination of $Rb_3Bi_2I_9$. *J. Alloys Compd.* **2000**, *296*, 53–58.

(5) Brgoch, J.; Lehner, A. J.; Chabinyc, M.; Seshadri, R. Ab Initio Calculations of Band Gaps and Absolute Band Positions of Polymorphs of $RbPbI_3$ and $CsPbI_3$: Implications for Main-Group Halide Perovskite Photovoltaics. *J. Phys. Chem. C* **2014**, *118*, 27721–27727.